Journal of Biomedical Optics 12(4), 044011 (July/August 2007)

Experimental evaluation of angularly variable fiber geometry for targeting depth-resolved reflectance from layered epithelial tissue phantoms

Adrien Wang
Vengadesan Nammalavar
Rebekah Drezek
Rice University
Department of Bioengineering
Houston Texas 77251-1892
E-mail: drezek@rice.edu

Abstract. The present study focuses on enhancing the sensitivity and specificity of spectral diagnosis in a stratified architecture that models human cervical epithelia by experimentally demonstrating the efficacy of using angularly variable fiber geometry to achieve the desired layer selection and probing depths. The morphological and biochemical features of epithelial tissue vary in accordance with tissue depths; consequently, the accuracy of spectroscopic diagnosis of epithelial dysplasia may be enhanced by probing the optical properties of this tissue. In the case of cellular dysplasia, layer-specific changes in tissue optical properties may be optimally determined by reflectance spectroscopy when specifically coupled with angularly variable fiber geometry. This study addresses the utility of using such angularly variable fiber geometry for resolving spatially specific spectra of a two-layer epithelial tissue phantom. Spectral sensitivity to the scattering particles embedded in the epithelial phantom layer is shown to significantly improve as the obliquity of the collection fibers increases from 0 to 40 deg. Conversely, the orthogonal fibers are found to be more sensitive to changes in the stromal phantom layer. [DOI: 10.1117/1.2769331]

Keywords: fiber optic probes; reflectance spectroscopy; epithelial dysplasia; phantom.

Paper 06368RR received Dec. 14, 2006; revised manuscript received Apr. 2, 2007; accepted for publication Apr. 14, 2007; published online Aug. 13, 2007.

1 Introduction

The use of reflectance spectroscopy for precancer detection[1–4] has generated increasing interest in the potential of depth-selective fiber geometry to probe and detect localized tissue pathology. This is especially true for tissue dysplasia associated with the development of incipient cancer. In this case, specific depth selection of diseased tissue could improve the identification of tissue dysplasia in the early stages by enhancing the discrimination between normal and abnormal tissue types. Varying the geometrical configurations of photon delivery and collection offers a promising means of achieving such depth selection. These configurations include the following: source-detector separation distances (SDSD),[5–7] aperture sizes,[8–12] numerical apertures,[8,10,13] spacing between the fiber probe and tissue surface,[8,9,14,15] and the angular orientation of fibers with respect to the target tissue.[16–18] The objective of all these geometrical manipulations is to enable the differentiation of superficially scattered photons from those multiply scattered at extensive depths. It is precisely by selectively enhancing and minimizing collections of photons originating from their respective target and background regions, that implementation of depth-resolved optical spectroscopy can be achieved.

Accordingly, the present study focuses on enhancing the sensitivity and specificity of spectral diagnosis in a stratified architecture that models human cervical epithelia by experimentally demonstrating the efficacy of using angularly variable fiber geometry to achieve the desired layer selection and probing depths. This is accomplished by: 1. accurately targeting the desired layer and then 2. successfully probing optical and physical characteristics of the targeted medium in a way that enables clinicians to make a proper spectral interpretation. The task is to target a specific tissue layer in such a way that the probed medium is more successfully characterized, both biochemically and morphologically. We believe that the proposed angularly variable fiber geometry should yield reflectance spectra that manifest such diagnostically relevant information about the specifically probed medium. It is equally important that the proposed fiber geometry minimize unwanted signals that may erroneously affect the characterization of the target tissue. Thus, the performance of angularly variable fiber geometry, with particular reference to its capability of producing diagnostically informative reflectance spectra, remains the subject of continued investigation.

To systematically address these issues in a controlled environment, we use a series of two-layer tissue phantoms to

---

Address all correspondence to Rebekah Drezek, Bioengineering, Rice University, PO BOX 1892, MS–142–6100 Main Street, Houston, TX 77005, United States of America; Tel.: 713–348–3011; Fax: 713–348–5877; E-mail: drezek@rice.edu

1083-3668/2007/12(4)/044011/14/$25.00

model human cervical epithelial tissue. The phantoms permit quantitative control of both physical and optical properties of the targeted medium. This allows us to selectively investigate a particular variable of phantom properties when the others are controlled as invariants. More precisely, by using the controlled phantoms, we are able to investigate the performance of fiber probes under different scattering and absorption conditions that are used to model the progression of epithelial dysplasia. We anticipate that the findings that result from the modeling in this study will serve as a foundation on which to conduct further investigations based on clinical observations from either *in-vitro* or *in-vivo* environments.

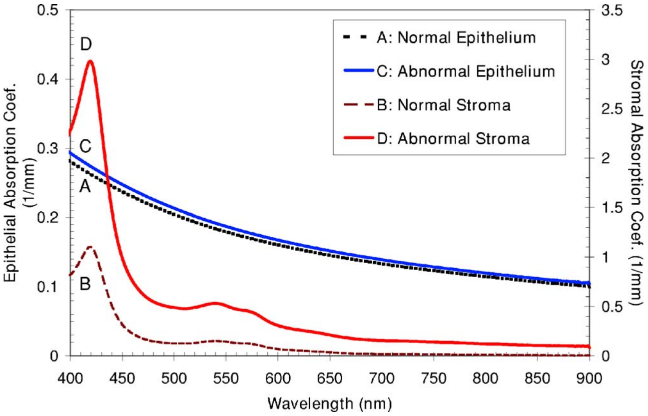

Fig. 1 (a), (b), and (c) The optical properties of the normal and abnormal epithelial phantoms that mark the boundary of the absorption and reduced-scattering coefficients implemented in the tissue phantoms. (c) depicts the reduced-scattering coefficients and anisotropies of the 0.51- and 0.92-μm polystyrene microspheres used in the basal layer.

2 Methods

2.1 *Tissue Phantom Geometry and Optical Properties*

Two-layer phantoms are used to mimic the structure of stratified cervical epithelium. The thickness of the epithelial (top) layer is set at 400 μm to approximate the average thickness of human cervical epithelia.[19] The stromal layer has a total depth of 25 mm to represent an optically semi-infinite tissue layer underneath the epithelium. The diameter of the cylindrical tissue phantoms is 22 mm, which is wide enough to encompass all optical paths collectible by our particular fiber geometry. A fine circular microscope cover glass (approximately 100 μm thick) separates the two phantom layers, and all contact joints are sealed with an optical-grade adhesive. The influence of the glass separator on photon propagation in the tissue phantoms is empirically determined to be negligible. This conclusion is based on the comparison between the reflectance spectra of a homogenous phantom (with only one layer) and a two-layer phantom that consists of the same properties as those of the single-layer phantom.[20] The reflectance spectra of the two phantoms are almost indistinguishable for all the fiber geometries under consideration in this study. It should be noted that the glass separator may enhance the effective thickness of the top phantom layer. However, since the thickness of the cover glass is reasonably small and optically transparent, we believe that its inclusion is a reasonable and necessary compromise in the development of this two-layer phantom structure.

The optical properties of human cervical epithelium are based on the values reported by Collier et al.,[21] Chang et al.,[22] and Drezek et al.[3] that were previously adopted by Zhu, Liu, and Ramanujam,[10] Wang et al.,[17] Skala et al.,[18] and Palmer and Ramanujam[23] in their respective studies on epithelial tissue. A wide range of tissue optical properties is implemented in our phantoms to ensure the comprehensiveness and validity of our study. The values for the reduced-scattering (μ_s') and absorption (μ_a) coefficients of the normal and abnormal epithelial phantoms can be found in Figs. 1(a) and 1(b), respectively. The reduced-scattering coefficients and anisotropies (g) of the phantoms are calculated with Mie theory, and the absorption coefficients are experimentally determined using a spectrophotometer.

2.2 *Fiber Geometry*

The configuration of the source and collection fibers is controlled with a mechanical stage that independently adjusts the fiber separation (SDSD) and fiber obliquity with respect to the phantoms. The SDSD is measured as the distance between the opposing edges of the source and collection fibers. Throughout this study, we maintain the source fiber at the orthogonal orientation and only investigate the angles of the collection fiber in relation to the target surface. Fiber separation and obliquity are tuned with micrometers, of which the operational uncertainties are smaller than 1 μm and 0.5 deg in magnitude, respectively. A circular cover glass is placed on the top of the phantoms to provide surface consistency, and the distal facets of the fiber optics are placed flush to the cover glass. Index matching between the fibers and cover glass is achieved with certified low-fluorescence immersion oil with a refractive index of 1.57 (Zeiss, Münich, Germany). The source and collection fibers, of which the core diameter and nominal numerical aperture are 200 μm and 0.22, respectively, are connected to a broadband light source (Ocean Optics, Dunedin, Florida HR2000) and spectrophotometer (Ocean Optics, Dunedin, Florida QE64000), respectively. All reflectance measurements are normalized to the reference reflectance of a 99% reflectance standard (LabSphere, North Sutton, New Hampshire) when measured with the orthogonal (0 deg) fiber. All reported reflectance spectra are sampled at three random locations on the phantoms and then averaged; the standard deviations with respect to the averages are within 5 percentage points for all measurements. For each measurement, five samples are automatically recorded and averaged with an integration time of 200 ms. To maintain phantom consistency, all phantoms are sufficiently agitated before each measurement.

2.3 *Phantom Properties and Rationale*

This study investigates the sensitivities of fiber probes to: 1. changes in epithelial scattering properties, 2. changes in stromal scattering properties, and 3. changes in tissue scattering and absorption coefficients of both phantom layers that simulate dysplastic progression in cervical epithelial tissue. Monodispersed polystyrene microspheres (Bangs and Polysciences Laboratories) and 10% intralipid emulsions (Sigma-Aldrich) are the sources of scattering for the phantoms. For each of the investigations reported, specific combinations of scattering particles are chosen to stimulate the progression of changes in scattering properties of either epithelial or stromal phantom layers with respect to developing epithelial dysplasia.

2.3.1 *Investigation 1: Changes in Epithelial Scattering Coefficients*

For investigation 1, we are interested in detecting the morphological variations of the scattering particles embedded in the phantoms' top (epithelial) layer. Generally speaking, in human cervical epithelia, a typical nucleus has a diameter of approximately 5 μm, while the effects of cellular dysplasia can nearly double the size. Instances involving an increase as large as 20 μm in diameter have also been reported.[2,16,24–28] Therefore, four sizes of microspheres are used to model the incrementally enlarging epithelial nuclei in pathologically progressing tissue. For our models, polystyrene microspheres 4.65 μm in diameter are used to simulate the cellular nuclei in a healthy epithelium; whereas polystyrene microspheres measuring 9.0 μm in diameter imitate those of the dysplastic cells in abnormal tissue. In addition, two intermediate sizes, 5.63 and 7.32 μm, represent the transitional stages between the normal and dysplastic cells. To simplify our models, only polystyrene microspheres are utilized in the epithelial layer to simulate the morphology of cellular nuclei. However, both polystyrene microspheres and intralipid emulsions are used to approximate the scattering properties of the underlying stromal tissue where the structural components are less morphologically defined. For these phantoms, two polystyrene microspheres, measuring 0.92 and 0.51 μm in diameter, are found to reasonably match the scattering properties of the stroma in normal and abnormal cervical tissue, respectively. Intralipid, as an emulsion of fatty molecules, also provides a good approximation to the scattering properties of the stromal tissue.

As described before, polystyrene microspheres of four different sizes are used to model the enlargement of epithelial nuclei caused by cellular dysplasia. Microspheres measuring 4.65 μm in diameter are diluted at a concentration of 7.7×10^7 particles per mL of water to approximate the scattering properties of normal cervical epithelia. The other microspheres, those measuring 5.63, 7.32, and 9.0 μm in diameter, are also prepared at the same concentration as the representations of increasingly dysplastic epithelia. Since the scattering properties of the epithelial layers are the sole subject of the current investigation, both morphological and optical properties of the stromal layers are kept constant. Polystyrene microspheres measuring 0.51 μm in diameter are diluted at a concentration of 5.5×10^{10} particles per mL of water for the stromal layers. As noted earlier, the four phantoms represent the transitional stages of progressively dysplastic epithelial tissue. For this reason, and because the properties of the stromal layer must be kept uniform in the context of this experimentation, the reduced scattering coefficients of the stromal phantoms are chosen to equal the medium of those of the normal and abnormal stroma, as shown in Fig. 1(b). In this section of our study, no extrinsic absorbers are added to allow targeting the effect of tissue scattering alone. Tissue absorption will be specifically addressed in an upcoming section, while a thorough investigation over a wide range of stromal scattering will be addressed in investigation 2.

2.3.2 *Investigation 2: Changes in Stromal Scattering Coefficients*

In healthy stromal tissue, collagen is abundant and provides strong background scattering. As dysplasia progresses, however, collagenous material underneath the affected region deteriorates, which diminishes its scattering strength.[29–33] Therefore, the changes in stromal optical properties, as a consequence of tissue dysplasia, also exert strong influence on photon propagation in tissue. In terms of scattering anisotropy, photons are scattered more isotropically in stroma than in epithelium. Typically, in the spectrum of visible light, the stromal anisotropies are approximately 0.8 to 0.85, while those of the epithelium are above 0.9. The stronger likelihood of backscattering due to its smaller anisotropies, along with the high scattering coefficients, make stroma a dominant source of tissue reflectance.

Two polystyrene-microsphere suspensions and two intralipid emulsions are prepared to emulate different conditions of stromal scattering properties. Categorized by the species of the scattering particles, four phantoms are created as follows: 1. 0.51- and 0.92-μm polystyrene microspheres at concentrations of 5.5×10^{10} and 1.2×10^{10} particles per mL of water, respectively, and 2. 0.3 and 0.6% emulsions of intralipid in water. The polystyrene phantoms have approximately equal reduced-scattering coefficients, but they differ in anisotropies: the 0.51-μm microspheres, by virtue of their smaller size, are more isotropically scattering than the 0.92-μm microspheres. The anisotropies and reduced-scattering coefficients of the 0.51- and 0.92-μm microspheres are calculated with Mie theory and shown in Fig. 1(c). Since the reduced-scattering coefficients (μ_s') are equated to the mathematical product of the scattering coefficients (μ_s) and 1 less the anisotropies ($1-g$), it is possible for two scattering particles to have similar reduced-scattering coefficients, even though their native scattering coefficients and anisotropies are different. Intralipid has the lowest anisotropies of the four basal phantoms, ranging from 0.87 to 0.52 in the visual near-infrared (VIS-NIR) wavelengths. The 0.3 and 0.6% intralipid emulsions approximate the lower and upper boundary values, respectively, of the stromal reduced-scattering coefficients, as shown in Fig. 1(b), while the reduced-scattering coefficients of the two polystyrene phantoms coincide with the medium of the boundary values. Using this particular combination of basal phantoms, we are able to investigate the influence of the concentrations (as in the intralipid phantoms) and anisotropies of the scattering particles (as in the polystyrene phantoms) to the resultant reflectance spectra. Uniform top layers are coupled with all four stromal phantoms. We use the 9.0-μm polystyrene microspheres, as previously noted, at the dilution of 7.7×10^7 per mL of water in the upper tissue phantom. No extrinsic absorbers are added to allow targeting of the tissue scattering effect alone.

2.3.3 *Investigation 3: Changes in Tissue Scattering and Absorption Coefficients Simulating Epithelial Dysplasia*

In the previous investigations, we focused on the effects of the scattering properties in tissue phantoms. In addition to scattering, tissue absorption is another essential element affecting reflectance spectra. For example, hemoglobin is a dominant chromophore in tissue that significantly affects the spectral signatures of tissue reflectance. Specifically, its predominant absorption may mask the spectral signals from other biological elements and consequently potentially distort the spectral diagnosis of tissue, especially when only nonvascularized tissue, such as the epithelium, is the target of interest. Therefore, as we examine the performance of depth-selective fiber geometry, the presence of hemoglobin absorption in the tissue phantoms must also be considered.

To perform experimentation under a more complete and realistic model of tissue, we implement four tissue phantoms with the inclusion of proper tissue absorptions in both epithelial and stromal layers. India ink and human hemoglobin are added to the epithelial and stromal layers, respectively, to simulate tissue absorption. Two of the phantoms resemble the tissue properties of normal and abnormal cervical epithelia that were previously shown in Fig. 1. In this protocol, polystyrene microspheres are used as the source of scattering in all tissue phantoms. For the normal tissue phantoms, polystyrene microspheres, measuring 4.65 and 0.92 μm in diameter, are used for the emulation of healthy epithelial and stromal layers, respectively, while the 9.0- and 0.51-μm polystyrene microspheres approximate the scattering properties of the abnormal epithelial and stromal tissue layers, respectively.

Two additional phantoms are prepared as the hybrids of the normal and abnormal tissue phantoms. The epithelial layers of the two original phantoms are interchanged to produce two additional permutations of the phantoms. By design, any pair of the original-hybrid phantoms differs in only one layer. To simplify the notations of the phantoms, the two original phantoms are labeled as *N-N* (normal epithelium and stroma) and *A-A* (abnormal epithelium and stroma) after the tissue properties that they model. The hybrid phantoms are marked as *N-A* and *A-N*, according to their respective epithelial-stromal combinations. Although the hybrid phantoms are entirely hypothetical in terms of their layer arrangements, they are specifically created to demonstrate that the proposed fiber geometry can achieve correct depth selections regardless of the compositions of the ambient layers.

3 Results

3.1 *Changes in Epithelial Layer Scattering*

This section investigates the ability of fiber probes to detect morphological variations of the scattering particles embedded in the phantoms' top layer. As previously noted, epithelial dysplasia is linked to the growth of epithelial nuclei. The enlarged nuclei in the epithelial layer, in turn, increase the local scattering coefficients of the affected region. More importantly, such changes in nuclear morphology may then result in reflectance spectra that may potentially yield diagnostically significant information about tissue pathology. Thus, to the extent that a given fiber geometry is able to respond to slight modifications in tissue pathology, the sensitivity and specificity of optical diagnosis of tissue pathology may, in fact, be improved.

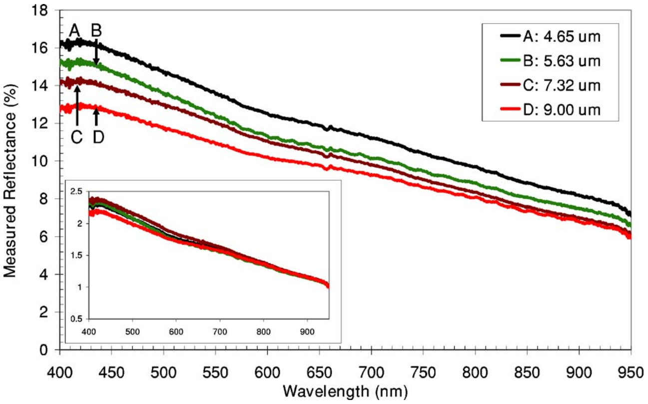

Fig. 2 Reflectance spectra detected by the 0-deg collection fibers at SDSD=500 μm when the dimension of the particles in the epithelial layer increases from 4.65 to 9.0 μm. The inset depicts the normalized spectra to demonstrate the congruence in spectral structures among the phantoms.

Figures 2–6 incorporate the reflectance spectra measured with various fiber angles and separations when only the epithelial (top) phantom layer is the subject of investigation. The properties of the phantoms correspond to the descriptions previously included in Sec. 2.3.1. Figure 2 shows the reflectance spectra of the four phantoms using the orthogonal fiber geometry (0-deg collection angle) at the SDSD of 500 μm. It can be seen that the reflectance levels of the spectra gradually diminish against the trend of increasing sizes of polystyrene microspheres embedded in the epithelial layer. However, this trend is no longer true when we reduce the fiber separation from 500 to 200 μm. For this fiber configuration (data shown in Fig. 3), the 4.65-μm microsphere phantom, which previously yielded the strongest reflectance, as shown in Fig. 2, now displays more subdued reflectance (third in magnitude; see Fig. 3) in relation to the other phantoms in the group. On the other hand, the 5.63- and 7.32-μm microsphere phantoms, which previously ranked as second and third in reflectance magnitude, respectively, now produce the two highest levels of reflectance with this orthogonal fiber geometry at a reduced SDSD. The significance of this transition is collectively explained in Sec. 4.1.

To increase the probing sensitivity to the superficial layer, we incrementally increase the collection fiber angle to 20, 30,

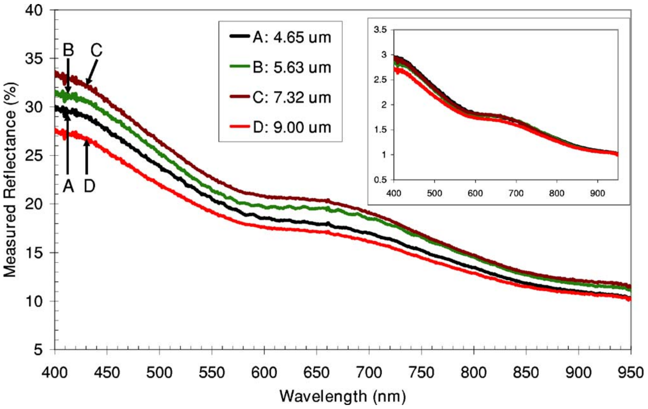

Fig. 3 Reflectance spectra detected by the 0-deg collection fibers at SDSD=200 μm when the dimension of the particles in the epithelial layer increases from 4.65 to 9.0 μm. The inset depicts the normalized spectra to demonstrate the congruence in spectral structures among the phantoms.

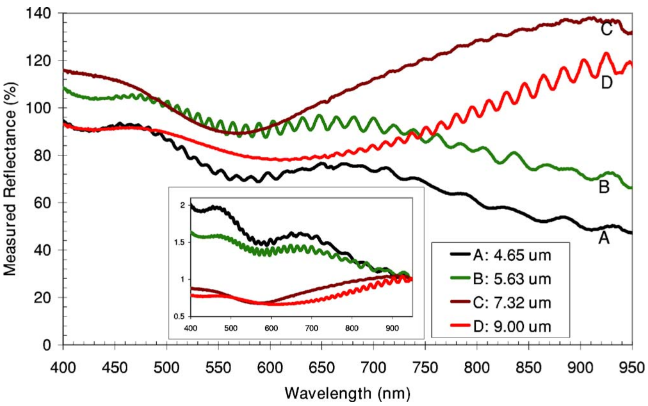

Fig. 4 Reflectance spectra detected by the 20-deg collection fibers at SDSD=200 μm when the dimension of the particles in the epithelial layer increases from 4.65 to 9.0 μm. The inset depicts the normalized spectra to demonstrate the spectral structures of the phantoms.

and 40 deg. Having the collection angle at 20 deg, with an SDSD of 200 μm, the spectral characteristics of the polystyrene microspheres embedded in the top layers become immediately apparent, as illustrated in Fig. 4. The oscillations, specific to the sizes of the microspheres, are also apparent. Despite the clear signs of top-layer scattering in the spectra, the influence of the basal-layer reflectance is still evident. More specifically, the depression and peak at about the 575- and 675-nm wavelengths, respectively, are still apparent in the spectra. The same characteristics in the spectral structures are also seen in Fig. 3, where the basal reflectance dominates. It should be noted that both the 4.65- and 5.63-μm microsphere phantoms show strong basal reflectance, which results from their low optical turbidity in the epithelial layer that allows an increased abundance of photons to reach the stromal layer.

One interesting observation of Fig. 4 is the reduced reflectance ripples for the 7.32-μm microspheres. The subdued oscillatory pattern of this particular phantom may be due to the cross-linker on the microspheres. This is true because, based on the results obtained from the scanning electron microscope and dynamic scattering spectroscopy, neither the morphological uniformity nor size dispersion (standard deviation =0.54 μm, or equivalently 7.2% with respect to the mean diameter) of the 7.32-μm microspheres is affected by the added surface cross-linkers. The size dispersions for the other polystyrene microspheres, specifically for sizes 4.65, 5.63, and 9.0 μm, are 0.63, 0.69, and 0.80 μm, respectively (equivalently, 13, 12, and 8.9% with respect to their mean diameters). Based on these numbers, the cross-linked 7.32-μm microspheres do not suffer increased size variability in comparison to the other particles used in this study. It should also be noted that the 7.32-μm microspheres have the smallest size dispersion of the group. Since all other microspheres with broader size distributions can produce perfectly visible scattering oscillations (Fig. 4), there is no logical reason to expect otherwise from the 7.32-μm microspheres if the size dispersion were the acting factor here. More importantly, in a separate measurement of cross-linked 4-μm microspheres, we have also observed similarly diminished scattering oscillations in comparison to plain 4-μm microspheres. Therefore, we believe that the surface chemistry of the cross-linked particles may cause the diminished oscillations in the reflectance spectra. In spite of the reduced ripples for the cross-linked particles, the use of the 7.32-μm microspheres is justifiable to best meet the objectives of our study.

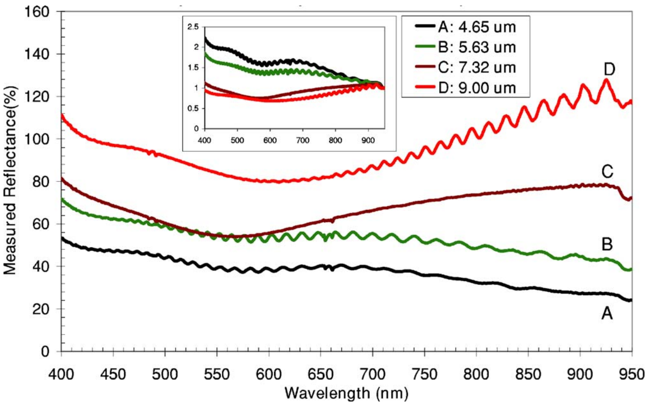

Fig. 5 Reflectance spectra detected by the 30-deg collection fibers at SDSD=200 μm when the dimension of the particles in the epithelial layer increases from 4.65 to 9.0 μm. The inset depicts the normalized spectra to demonstrate the spectral structures among the phantoms.

To further diminish the influence of basal-layer reflectance, we increase the collection angle to 30 deg, at which angle we simultaneously observe significantly enhanced scattering characteristics of the polystyrene microspheres in the top layer. That is, as the collection angle increases to 30 deg, the sequence of reflectance magnitude is at once aligned with the scattering intensities of the superficial layer, as shown in Fig. 5. In addition, the previously observed spectral depressions and peaks, at their respective wavelengths of 575 and 675 nm, are strongly suppressed. Significantly, the two prior results demonstrate that the 30-deg collection fiber has sufficiently overcome the influence from the stromal layer and is predominantly sensitive to the scattering environments at superficial depths.

Figures 6(a) to 6(d) demonstrate the spectral progression of the phantoms measured with different fiber angles in the form of normalized reflectance spectra. The characteristics of the stromal-layer scattering particles, such as the valleys and peaks seen in Figs. 3 and 4, gradually disappear as the degree of fiber obliquity increases. For both the 4.65- and 5.63-μm microsphere phantoms, the low scattering coefficients of the epithelial layers, and resulting strong stromal layer reflectance, combine to permit a strong presence of stromal reflectance in the spectra so that the stromal signal only begins to phase out from the spectra when the collection angle reaches 35 deg. In contrast, the 7.32- and 9.0-μm microsphere phantoms yield virtually identical spectra when the collection angle only increases to 20 deg. Since the spectral structures of these particular phantoms are virtually invariant for fiber angles beyond 20 deg, we conclude that a distinct layer separation can be realized for the 7.32- and 9.0-μm microsphere phantoms at a fiber angle of 20 deg or more.

3.2 *Changes in Stromal Layer Scattering*

Figure 7 shows the reflectance spectra sampled with the 0-deg fiber at the SDSD of 500 μm. This configuration yields prob-

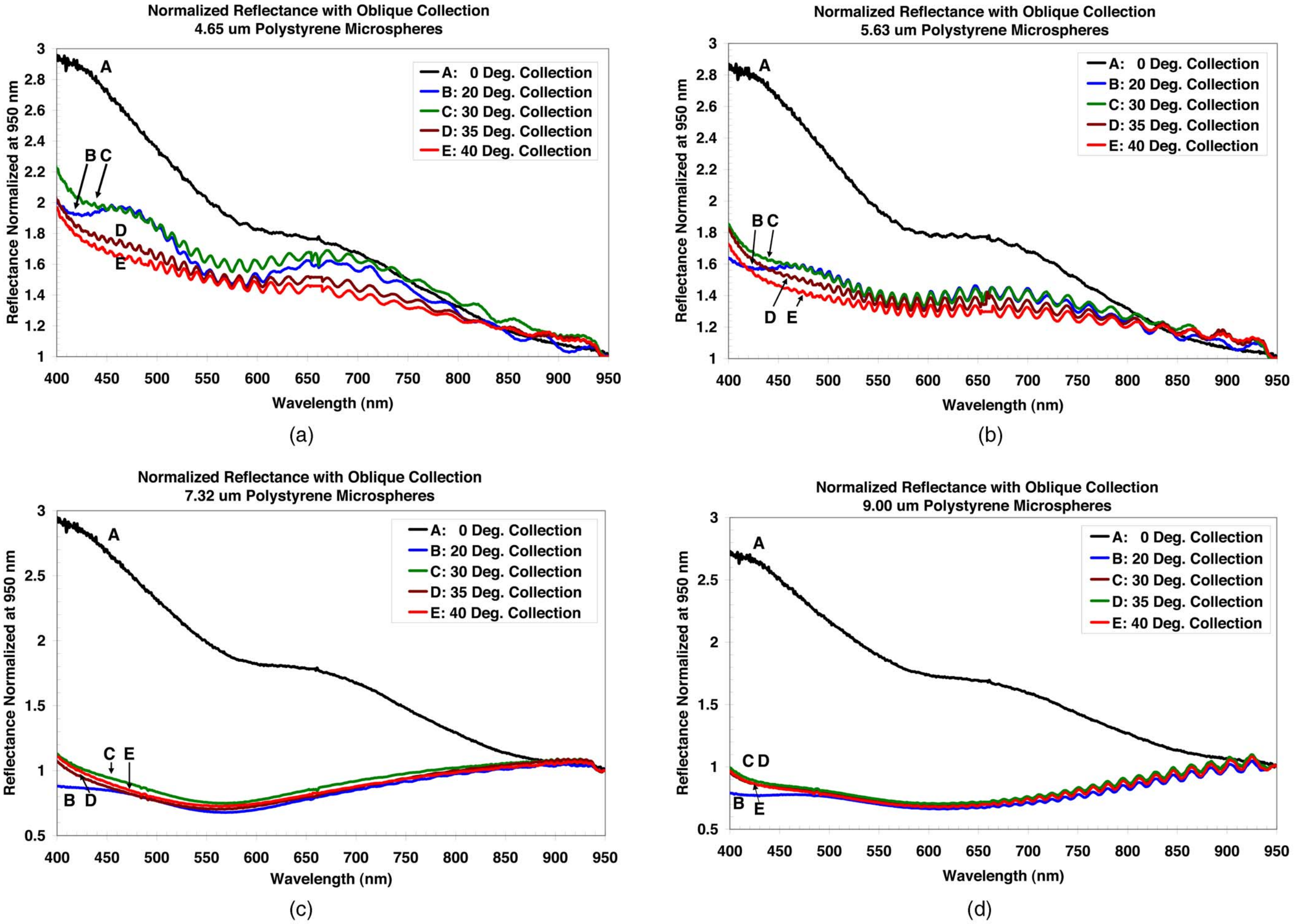

(a) (b) (c) (d)

Fig. 6 (a) to (d) Reflectance spectra, equalized to 1 at 950 nm, of the two-layer phantoms, with microspheres of sizes 4.65, 5.63, 7.32, and 9.0 μm, detected with increasing collection angles, demonstrating spectral differences between orthogonal and oblique fiber geometries. Phantoms with stronger upper-layer scattering, or larger particles, in this case, show faster structural convergences with increasing fiber obliquity. The fiber separation, measured edge to edge, is 200 μm for all data shown.

ing depths into the second phantom layer sufficient to resolve the difference in stromal scattering properties among the phantoms. A considerable disparity in the reflectance levels, as a result of the difference in intralipid concentration, is seen. In addition, the normalized reflectance spectra are also noticeably disparate between the two intralipid phantoms (see the inset of Fig. 7). More specifically, the 0.6% intralipid emulsion, because of its larger scattering coefficients, has a nearly flat reflectance spectrum, while the 0.3% intralipid emulsion yields relatively stronger reflectance in the blue region of the spectrum. However, we observe a change in the spectral structure of the intralipid reflectance when the fiber separation is reduced to 200 μm (see Fig. 8). First, the reflectance spectrum of the 0.6% intralipid emulsion no longer appears to be flat. In addition, the intensity levels of the reflectance yielded by the intralipid phantoms are in better agreement with the 1:2 ratio of the emulsions (0.3 to 0.6%). Furthermore, the normalized spectra of the two phantoms, as shown in the inset of Fig. 8, are more structurally congruent, in that the normalized spectra virtually overlap each other for wavelengths longer than 550 nm. Consequently, the remnant disparity is only observable at the shorter end of the spectrum where the probing depths of the fibers are still too deep to effectively account for all superficially scattered rays in the 0.6% intralipid phantom. The significance of these observations relating fiber geometry and intralipid concentration in the basal layer of the phantoms is extensively analyzed in Sec. 4.2.

Returning to Figs. 7 and 8, we investigate another set of phantoms that incorporates 0.51- and 0.92-μm polystyrene microspheres as the source of scattering from the stromal layers of the tissue phantoms. Beginning with the 0-deg fibers separated with the SDSD of 500 μm (data shown in Fig. 7), a fiber configuration that is expected to probing extensively into the phantoms, we observe that the reflectance difference between the 0.51- and 0.92-μm microsphere phantoms is generally only discernable at wavelengths greater than 750 nm. More interestingly, the two spectra intersect at approximately 550 nm, at which wavelength junction the reduced-scattering coefficients of the two phantoms are nearly identical [Fig. 1(c)]. On the other hand, when the fiber separation is reduced to 200 μm, the 0.51-μm microsphere phantom renders stronger reflectance than the one that consists of the 0.92-μm microspheres in its stromal layer at the shorter fiber separation.

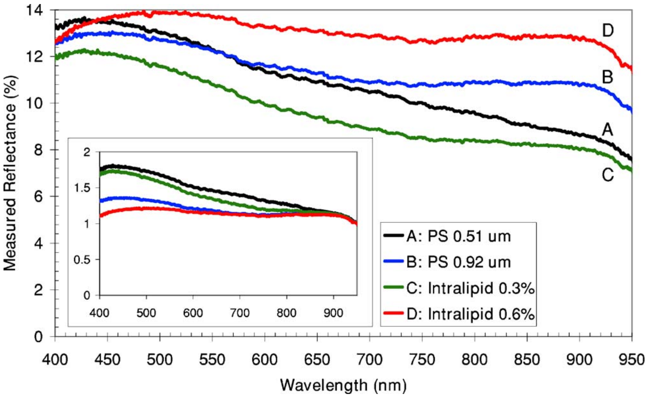

Fig. 7 Reflectance spectra detected by the 0-deg collection fibers at SDSD=500 μm for various stromal scattering particles. The inset depicts the normalized spectra to demonstrate spectral structures of the phantoms that reflect the characteristics of the scattering coefficients and anisotropies of the basal layer.

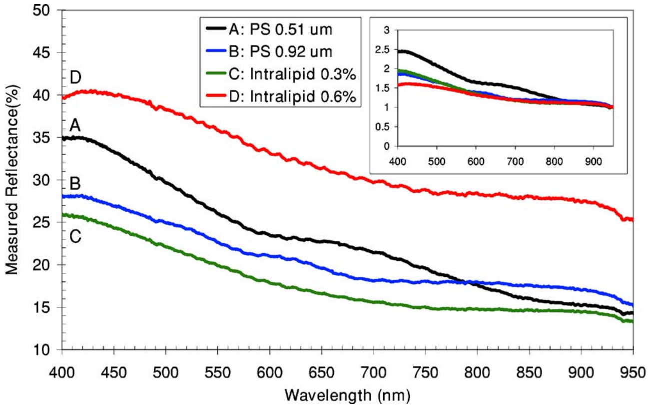

Fig. 8 Reflectance spectra detected by the 0-deg collection fibers at SDSD=200 μm for various stromal scattering particles. The inset depicts the normalized spectra to demonstrate spectral structures of the phantoms that reflect the characteristics of the scattering coefficients and anisotropies of the basal layer.

Similar to the results shown in Sec. 3.1, as we modify the collection angle to 20, 30, and 40 deg, the characteristics of the top phantom layers become more apparent (Fig. 9). Also, the oscillatory spectral patterns become more prominent as the fiber angle increases, and the spectral congruence among the curves is inversely dependent on the strength of basal scattering. The 0.3% intralipid yields the fastest convergence in terms of reflectance intensity as the fiber obliquity increases, whereas the 0.6% intralipid is the slowest. For demonstrative purposes, Fig. 10 shows that good conformities in both reflectance levels and spectral characteristics, specific to the epithelial phantom layers, are achievable with the 40-deg collection angle, regardless of the different scattering compositions used in the stromal phantom layers.

3.3 *Changes in Tissue Scattering and Absorption Simulating Epithelial Dysplasia*

As extensively detailed in Sec. 2.3.3, four tissue phantoms, which include hemoglobin, are created to investigate the performance of depth-selective fiber geometry. Six fiber configurations, to include (0-deg collection at 200- and 500-μm SDSDs); (20-deg collection at 200- and 500-μm SDSDs); and {40-deg collection at 200-, and 500-μm SDSDs}; are used for the reflectance measurements.

Figure 11 shows the reflectance collected from these phantoms using the 0-deg collection fiber with 500-μm separation. Using the orthogonal geometry and a large fiber separation of 500 μm, a configuration expected to produce extended probing depths, phantoms that have different stromal layers are well differentiated in the reflectance spectra, while the spectra of phantoms with common stromal layers, such as the *N*-*N*, *A*-*N*, and *A*-*A*, *N*-*A* pairs, bear strong resemblances in both reflectance level and spectral structure. For this particular fiber geometry, this result suggests that differences in the epithelial layers do not affect the overall reflectance measurements. However, we have demonstrated that more superficially sensitive probing can be achieved by reducing the fiber separation distance to 200 μm. Figure 12 and its inset show that a reduction in probing depths does result in stronger spectral sensitivities to the epithelial phantom layers. This is supported by comprehensive evidence that: 1. the reflectance valley induced by hemoglobin's Soret absorption (at 415 nm), in relation to the whole spectrum, is reduced—a result that signifies a relative decrease in hemoglobin absorption; 2. the proportion of reflectance in the blue region of the spectrum has increased—an indication of increased detection of superficially penetrating photons; and 3. the spectra, which previously correlated solely to the stromal compositions of thephantoms, now display significant distinctions, even for phantoms with common stromal layers.

The spatial balance of the collected reflectance shifts toward the superficial layer whenever increasingly oblique collection angles are used. The 20-deg 500-μm fibers have reflectance spectra similar to those of the 0-deg 200-μm fibers. Since the general observations made for the 20-deg 500-μm fibers are consistent with those for the 0-deg 200-μm fibers, the graphical data are not repeated here. A more interesting result comes from the 20-deg 200-μm fiber pairs, of which the reflectance spectra simultaneously exhibit dual characteristics of both tissue layers. In all the spectra shown in Fig. 13, the fine oscillatory spectral patterns, specific to the types of polystyrene microspheres embedded in the epithelial phantom layers, are visually distinguishable, while the coarse structures of the spectra are commonly shared by phantoms with the same stromal layers.

It is apparent that layer separation in the reflectance spectra correlates to the degree of fiber obliquity; thus, the use of a more obliquely oriented collection fiber will, correspondingly, achieve a more definitive separation of the layers in the reflectance spectra. The results shown in Fig. 14 demonstrate that the 40-deg. fiber with 200-μm SDSD is sufficiently capable of resolving the morphology of the epithelial scattering particles and eliminating the hemoglobin interferences from the basal layers. The 40-deg 500-μm fibers share similar characteristics with the 20-deg 200-μm fibers, and thus are not repeated here. In Fig. 14, the oscillatory patterns, specific to their respective polystyrene microspheres embedded in the epithelial layers, are clearly resolved. In addition, signs of hemoglobin absorption, especially at the Soret (415 nm) and

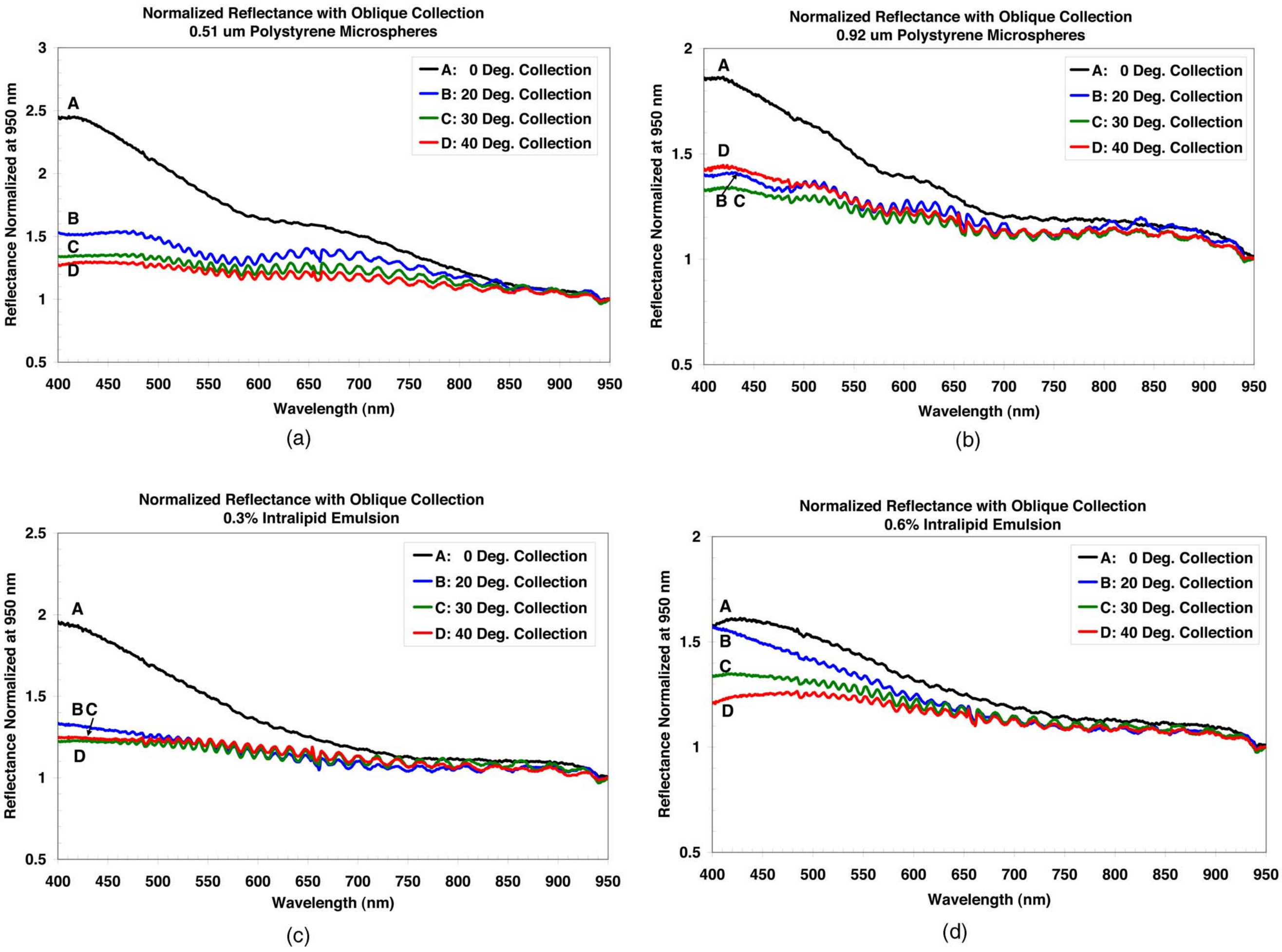

Fig. 9 (a) to (d) Reflectance spectra, equalized to 1 at 950 nm, of the two-layer phantoms, with 0.51- and 0.92-μm polystyrene microspheres and 0.3 and 0.6% intralipid emulsions in the basal layer, detected with increasing collection angles, demonstrating spectral differences between orthogonal and oblique fiber geometry. Phantoms with greater basal-layer scattering show faster structural convergences with increasing fiber obliquity. The fiber separation, measured edge to edge, is 200 μm for all data shown.

Q-band wavelengths (540 and 580 nm), are strongly suppressed.

4 Discussion

4.1 *Depth-Resolved Reflectance: Sensitivities to Morphological Variations in the Superficial Layer*

From the results presented in Sec. 3.1, particularly for the orthogonal fiber geometry with 500-μm SDSD, we observed an opposing trend in the intensity level of the reflectance spectra with respect to the scattering coefficients of the epithelial phantom layer. The diminishing reflectance levels, together with the opposing phenomenon of increasing epithelial scattering due to enlarged scattering particles, lead to the conclusion that this particular fiber geometry might be predominantly sensitive to the stromal phantom layer, rather than the epithelial layer. This is true because, with greater epithelial scattering in the phantoms, it is likely that more photons are scattered and reflected at shallow depths and thus not detected by the collection fiber situated far from the illumination point. By the same argument, the rise in superficial scattering should reduce the number of photons that reach the stromal layer, from which this particular fiber configuration gathers the majority of its reflectance signal. As a consequence, the diffuse reflectance originating from the stromal layer decreases, which results in the diminishing reflectance levels we observe. The increase in the number of early-returning photons, caused by the rise in epithelial scattering, is not seen here because the extended SDSD precludes the collection of photons that are reemitted from shallow tissue depths. There is more evidence to indicate that this particular fiber geometry cannot differentiate the enlarging scattering particles in the top layer. Specifically, and importantly, among the four phantoms, the reflectance levels only differ within 3 percentage points, which indicates that it is difficult to differentiate among the four phantoms based on the intensity levels of the reflectance spectra. Furthermore, the spectral characteristics, as shown in the inset of Fig. 2 in the form of normalized reflectance spectra, are nearly uniform. This indicates that the reflectance spectra share similar properties and are of the same origin (the stromal phantom layer). The results shown in

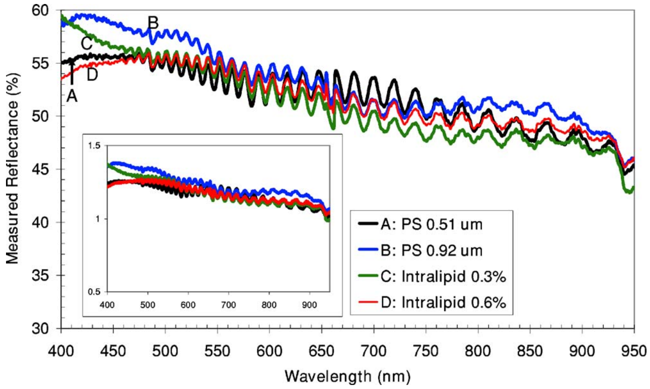

Fig. 10 Reflectance spectra detected by the 40-deg collection fibers at SDSD=200 μm when different stromal scattering particles are used. The inset depicts the normalized spectra to demonstrate the congruence in spectral structures among the phantoms. Similar spectra are seen regardless of the composition of the basal layers.

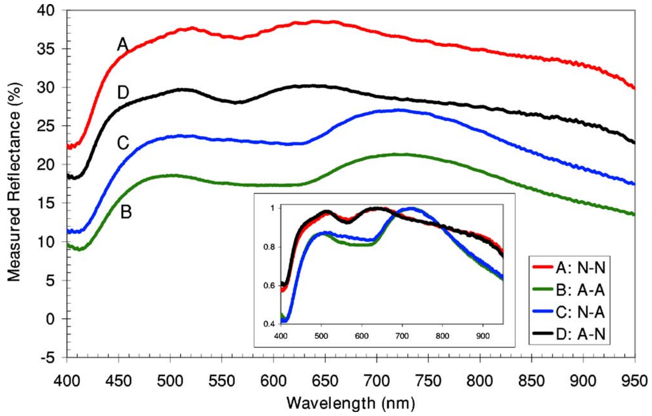

Fig. 12 Reflectance spectra detected by the 0-deg collection fibers at SDSD=200 μm with respect to different combinations of phantom layers. For this deeply probing fiber geometry, phantoms sharing common basal layers yield similar spectral structures. The reflectance levels are strongly influenced by the scattering properties of the upper phantom layers; however, the difference in the upper layer is not reflected in the normalized spectra.

Fig. 2 give little indication of the enlarging scattering particles in the epithelial layer, while all other evidence suggests a uniform origin of the reflectance spectra. This affirms our expectation of a deeply probing fiber geometry characterized by minimal sensitivity to the epithelial layer.

Thus, to execute a more superficially sensitive reflectance measurement using the orthogonal fiber geometry, the SDSD is reduced to 200 μm. For this fiber configuration, we find some evidence, as shown in Fig. 3, which suggests increased probing sensitivity to the upper layer. Specifically, we observed a shift in the levels of reflectance from the phantoms detectable by the fibers when the SDSD is reduced from 500 to 200 μm. From the data reported in Sec. 3.1, the 4.65-μm microsphere phantom, which yields the strongest reflectance when the SDSD is 500 μm, displays more subdued reflectance (third in magnitude relative to the other phantoms) when the SDSD is reduced to 200 μm. The significant decrease in reflectance of the 4.65-μm microsphere phantom is expected for this particular fiber geometry. This is because the 4.65-μm microspheres offer the lowest epithelial scattering coefficients of the phantom group; consequently, the number of reflected photons from the epithelial layer for the same phantom is also expected to be lowest. In addition, as the sensitivity of the fiber probe shifts toward the epithelial layer, the determination of the overall reflectance no longer solely depends on the reflectance from the stromal phantom layer. Consequently, with the combined effect of minimal epithelial photons and lessened sensitivity to the stromal layer, the strength of reflectance of the 4.65-μm microsphere phantom decreases significantly in comparison to the other phantoms. On the other hand, the phantom with the 9.0-μm microspheres in its top layer represents the opposite extreme where the increase in superficial-layer scattering, which strongly attenuates the number of photons penetrating to the stromal layer, does not sufficiently compensate for the reduction in

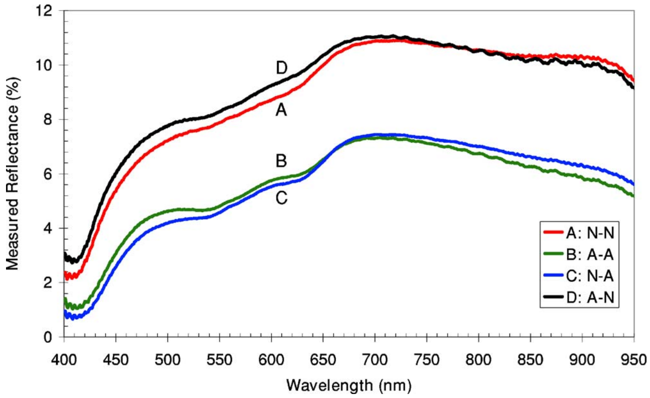

Fig. 11 Reflectance spectra detected by the 0-deg collection fibers at SDSD=500 μm with respect to different combinations of phantom layers. For this deeply probing fiber geometry, phantoms sharing common basal layers yield similar reflectance spectra in both reflectance levels and spectral structures. The difference in the upper layer is not clearly resolved by this fiber geometry.

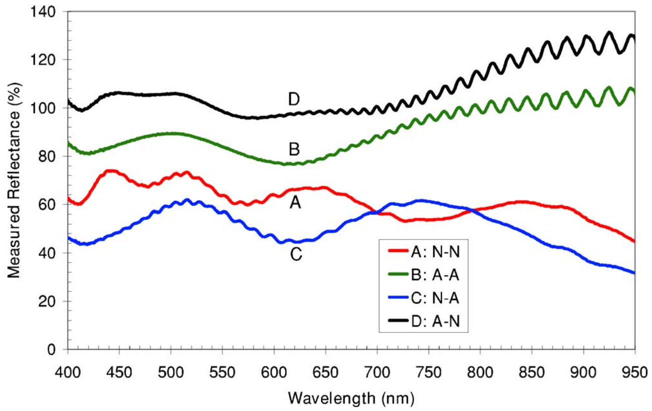

Fig. 13 Reflectance spectra detected by the 20-deg collection fibers at SDSD=200 μm with respect to different combinations of phantom layers. Fine oscillatory patterns specific to the microspheres embedded in the upper layer can be seen in their respective phantoms. The coarse structures of the overall spectra still largely depend on the composition of the basal layer. The grouping of the spectra has been swapped for this superficially probing fiber geometry.

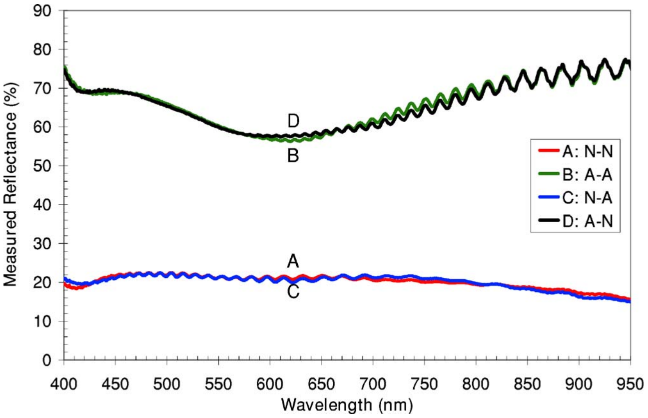

Fig. 14 Reflectance spectra detected by the 40-deg collection fibers at SDSD=200 μm with respect to different combinations of phantom layers. Definitive oscillatory patterns specific to the microspheres embedded in the upper layer can be seen in their respective phantoms despite the phantom composition in the basal layers.

basal reflectance. This is because a large proportion of the fibers' sensitivity still resides in the stromal layer for the orthogonal fiber geometry. Not surprisingly, the intermediate levels of epithelial scattering of the 5.63- and 7.32-μm microspheres should and did result in the maximal detection of the overall reflectance. This conclusion may be explained by the presumption that these microspheres would necessarily augment reflectance originating from the epithelial layer before excessively reducing light reflected from the stroma. This indicates that the dual reflectance contribution from both the top and bottom layers of the phantoms can be attributed to the orthogonal fiber configuration when the SDSD is small. Although the intensity of the reflectance spectra is affected by the scattering coefficients of the epithelial phantom layer, as discussed before, the spectral structures of the normalized spectra, as shown in the inset of Fig. 3, remain uniform. The uniformity of spectral structure implicates a singular dominant source of the reflectance for all four phantoms. Since the only common denominator among the phantoms is the invariant stromal layer, we conclude that the orthogonal fiber geometry predominantly interrogates the stromal layer and does not sufficiently resolve the enlarging scattering particles at superficial depths.

Using the 20-deg fiber (Fig. 4), the 7.32-μm microsphere phantom exhibits the highest reflectance, even though the 9.0-μm microsphere phantom has the highest epithelial scattering coefficients among the four phantoms. This phenomenon may also be attributed to the dual-layer probing of the fiber. While the 9.0-μm microspheres supply the strongest reflectance from superficial depths, the correspondingly converse effect of reducing basal reflectance is also significant. As the 20-deg fiber still collects reflectance from both phantom layers, the reduction in stromal-layer reflectance still negatively affects the overall reflectance level of the 9.0-μm microsphere phantom. However, as the fiber angle continues to increase, the resultant reflectance spectra become more characteristic of the scattering microspheres embedded in the epithelial layer. More specifically, at the collection angle of 30 deg, the sequence of reflectance magnitude agrees with the increasing trend of epithelial scattering coefficients in the top phantom layers. Furthermore, the stroma-specific spectral depressions and peaks, particularly observable at the wavelengths of 575 and 675 nm, are strongly suppressed in the data shown in Fig. 5. The combined results indicate that the reflectance signal from superficial depths can be effectively enhanced, even in the presence of a dominant reflectance source, such as the stromal layer implemented in our phantoms.

4.2 *Depth-Resolved Reflectance: Sensitivities to Changes in the Morphology of the Scattering Elements in the Basal Layer*

From the results presented in Sec. 3.2, particularly for those involving the intralipid phantoms, we observed that the spectral structures and intensity levels of the reflectance spectra vary significantly with respect to fiber geometry. Beginning with the orthogonal fiber with SDSD of 500 μm, the high scattering of the 0.6% intralipid emulsion produces reflectance that is evenly distributed across the spectrum in spite of the fact that photons are more intensely scattered at shorter wavelengths. This preferential enhancement of the long wavelengths is most logically attributed to the particular fiber geometry that is in use. When the SDSD is sufficiently extensive, the rise in the number of photons reflected near the source fiber is less detectable to the collection fiber, which is particularly sensitive to deeper depths of the phantom. Therefore, photons near the blue end of the spectrum, although they are in fact more intensely scattered and reflected nearer the phantom surface than those near the NIR region, do not proportionally contribute an equal gain in reflectance as do their counterparts in the NIR. Consequently, the spectral structure flattens when the intralipid concentration increases from the 0.3 to 0.6% emulsion. The measured reflectance spectra further support this analysis when the fiber separation decreases to 200 μm (data shown in Fig. 8), since the fiber geometry becomes more sensitive to superficially scattered photons at shallower depths. More specifically, the intensity levels of the reflectance yielded by the intralipid phantoms are in better agreement with the 1:2 ratio of the emulsions (0.3 to 0.6%). This indicates that the effect of omitting superficially scattered photons of the blue wavelengths, as a result of the higher phantom scattering coefficients, is not as pronounced as in the previous instance where the reflectance levels of the intralipid phantoms are very similar (differing by less than a percentage point) at the 400-nm wavelength. The greater sensitivity to shorter spectral wavelengths suggests that reduction in SDSD does, indeed, moderately lift the probing focus of the fiber probe from the deep stromal layer toward the phantom surface.

The intralipid phantoms allow us to test the capability of fiber probes to resolve concentration differences, while the polystyrene phantoms, namely those with the 0.51- and 0.92-μm microspheres in the basal layers, are more useful for examining reduced-scattering coefficients and anisotropies. The anisotropy is of great interest to us because it is strongly dependent on the morphology of the scattering elements. For example, the anisotropy of spherical particles is correlated to the sizes of the particles: particles greater in size typically have anisotropies in favor of the forward direction (thus, of values nearer to 1), while smaller particles are generally less forward scattering. Since these two phantom types have similar reduced-scattering coefficients (μ_s'), it should be noted that the 0.92-μm polystyrene phantom has greater scattering coefficients in the natural form (μ_s) than the 0.51-μm phantom, because the anisotropy factors (g) of the former are also greater. Taking these findings into consideration, we believe that the reduced-scattering coefficients are a more descriptive metric to describe the scattering properties of the phantoms when the fiber geometry is primarily sensitive to deeper depths. Under these circumstances, the mathematical models of diffuse reflectance and the use of reduced-scattering coefficients in the description of bulk reflectance are better observed. In contrast, when the fiber geometry is more sensitive to superficial scattering, anisotropic scattering is specifically amplified in the determination of reflectance spectra. Under this set of circumstances, large angular deflections, during the propagation of scattered photons, are relevant.[13] In other words, the 0.51-μm microsphere phantom, by virtue of its smaller anisotropies, is expected to produce markedly stronger reflectance than the 0.92-μm microsphere phantom when the fibers' probing depths are superficial. Conversely, both of the microsphere phantoms would generate reflectance of similar magnitude when the fibers' probing depths are sufficiently deep.

The results presented in Sec. 3.2 confirm our hypothesis stated earlier. More specifically, the reflectance difference between the 0.51- and 0.92-μm microsphere phantoms is generally discernable only at wavelengths greater than 750 nm when the orthogonal fiber geometry with 500-μm SDSD is used. More interestingly, the two spectra intersect at approximately 550 nm, at which wavelength junction the reduced-scattering coefficients of the two phantoms are nearly identical [Fig. 1(c)]. Beyond 550 nm, the reduced scattering of the 0.92-μm microsphere phantom is slightly greater than that of the 0.51-μm microsphere phantom, and this trend is correspondingly manifested in the spectra. A logical explanation may be that the 0.92-μm microsphere phantom, with its forward-scattering anisotropies and higher values in both the native- and reduced-scattering coefficients, yields particularly strong basal reflectance at deeper depths that are preferentially detected by the 0-deg 500-μm SDSD fiber configuration. While these matching observations could be merely coincidental, information obtained from the data cited in Fig. 8 strengthens our belief that the prominence of the anisotropy in the determination of reflectance increases as the fiber geometry becomes more sensitive to superficially scattered photons. The data given in Fig. 8 show that the 0.51-μm microsphere phantom renders stronger reflectance than the one that consists of the 0.92-μm microspheres in the stromal layer at 200-μm SDSD. It results from the natural tendency of photons to be backscattered by smaller particles, and the anisotropic scattering effect may offset the greater scattering power of the larger particles and push the intersection of the two spectra from 550 nm, as previously shown in Fig. 7, to nearly 800 nm. At longer wavelengths, where the probing depths of the fibers are sufficiently deep, the reflectance detection remains preferential to the 0.92-μm microsphere phantom, of which the higher anisotropies direct more photons forward into the medium, resulting in higher reflectance from the stromal layer. Based on our experimental observations, we believe that the anisotropies of the scattering particles in the phantoms could have a strong influence over the spectral dependence of the reflectance, especially at superficial probing depths where the phenomenon of backscattering dominates.

4.3 *Depth-Resolved Reflectance: Tissue Phantoms with Relevant Tissue Scattering and Absorption*

Based on the results shown in Sec. 3.3, we observed that the orthogonal fiber geometry with extensive SDSD is able to differentiate the phantom properties of the stromal layer, whereas the difference in the epithelial phantom layer does not affect the overall reflectance spectra. However, as the SDSD is reduced to 200 μm, we begin to observe the epithelial influence in the overall spectra. This result agrees with the conclusion drawn in our previous discussion: that the SDSD indeed has significant effect on the spatial distribution of the reflectance measurements. Based on the results shown in Fig. 12, we see a relative decrease in the reflectance intensity of phantoms with abnormal epithelial layers when compared to their counterparts with normal epithelial layers. This suggests that the influence from the epithelial layers may require consideration in the overall interpretation of the reflectance spectra. Specifically, since the scattering coefficients of the abnormal epithelium are 2.5 times higher than those of the normal epithelium, the probability of photons being superficially reflected from depths outside the detection of the collection fiber is then also higher. The stronger epithelial scattering, which reduces the number of photons reaching the stromal layer, consequently diminishes the reflectance originating from greater depths. However, despite the difference in reflectance due to the variations in the epithelial layers, the more interesting observation is that the normalized spectra of the phantoms with common stromal layers remain congruent. This finding indicates the inadvisability of using flush fibers to isolate the signals from superficial tissue depths in as much as the stromal layers remain a dominant part of the overall reflectance.

As the collection angle continues to increase to 40 deg, we are able to achieve complete layer separation by demonstrating that the reflectance spectra sampled by the 40-deg fibers only correlate to the epithelial phantom layers. This finding, as well as the results presented in Secs. 3.1 and 3.2, all affirm the viability of using the angled-fiber approach to correctly characterize tissue with respect to particular layers of interest.

4.4 *Comparisons to Published Work on Spatially Resolved Spectroscopy*

In recent years, the importance of spatially resolved spectroscopy has gained much interest. From Monte-Carlo-based computational analyses to clinical measurements, many different approaches have been proposed to achieve desired depth selection in stratified tissue structures. More specifically, with respect to fiber geometries, the commonly adopted approaches are fiber separation (SDSD) and angles. Amelink et al.,[34,35] in their differential path-length spectroscopy study, demonstrated the feasibility of achieving analysis of particle size in superficial layers of turbid media by sampling diffuse reflectance at different fiber separations, followed by a post-measurement algorithm to compute the superficially scattered reflectance signals. Other studies on the approach of SDSD have also demonstrated that large fiber separations consistently produce extensively diffused reflectance and deeper probing depths.[17,36] More specifically, Arifler et al.[36] demonstrated an increasingly significant influence of hemoglobin absorption to the overall reflectance spectra as SDSD increases. Their result is consistent with the observations made in our study, particularly in Sec. 3.3.

In addition to SDSD, the approach of utilizing variable fiber angles to achieve spatially resolved spectroscopy has also been demonstrated. One advantage of the angular approach is its ability to further enhance the detection of superficially scattered light. As shown in this study, superficially scattered reflectance can be directly measured with angled fibers without further signal processing. Liu and Ramanujam,[37] and Skala et al.[18] have also shown the possibility of detecting enhanced fluorescence signals from epithelial phantom layers as the illumination angle increases from 0 to 45 deg. Another interesting approach, while similar in principle to our angled fiber geometry, uses a ball lens-coupled fiber probe instead of rotating fibers for depth-resolved spectroscopy of epithelial tissue.[15,38] By adjusting the focal point of the ball lens, the illumination and collection angles are effectively manipulated. Thus, enhanced epithelial fluorescence and reflectance measurements are demonstrated in both computational prediction and phantom experimentation. Neiman et al.[16] showed that the applicability of the angled fiber approach can be further improved when polarization gating is integrated in the fiber probe to provide more refined spatial resolution for superficially scattered signals.

While the geometric manipulation of fiber probes is indeed an effective means of achieving more refined spatial resolution in turbid media, the spatial selectivity of this approach ranges from 50 to a few hundred micrometers,[17,39] whereas the spatial resolutions of optical coherence gating and confocal imaging are approximately 10 to 15 μm. However, this simple fiber geometry manipulation does provide sufficient spatial selectivity for spectroscopy where the spatial requirement is relatively minimal. Fiber geometries and their effectiveness for spatial selection are expected to significantly improve the efficacy of current spectroscopic diagnostics with limited additional implementation complexity and cost, which will result in accurate, fast, and portable optical diagnostics in the future.

5 Summary

The evidence for achieving spatially resolved reflectance measurement using angularly variable fiber geometry is demonstrated. Combined with fiber separation, sufficient layer separation is carried out in experimentation using tissue phantoms with a wide range of optical properties. Generally speaking, an increase in fiber obliquity with respect to the target surface at small source-detector separation distances yields significant sensitivity to the superficial region of the target. Notwithstanding these findings, the spatial specificity of fiber geometry also depends on the scattering and absorption properties of targeted regions in a turbid medium. By adopting a two-layer stratified epithelial tissue model, this study specifically assesses the effects of layered distribution of tissue scattering and absorption to the spatial resolution of reflectance sampling using angularly variable fiber geometry.

Using the two-layer phantoms, we obtain strong experimental evidence that the morphological variations of the scattering particles embedded in the epithelial phantom layers do not directly result in discernable changes in the reflectance spectra when the orthogonal fiber geometry is used. On the contrary, by observing the spectral transitions of the reflectance spectra sampled using different fiber configurations, as collectively demonstrated in Figs. 1 and 5, it is evident that the oblique fiber geometry accentuates the spectral characteristics of the scattering elements in the epithelial phantom layer. At the same time, the stromal influence to the overall spectra is much suppressed. Thus, as a result of the improved layer separation, one can differentiate among the phantoms by directly comparing reflectance levels and spectral patterns of the reflectance spectra when the oblique fibers are implemented. However, when the stromal properties are varied in the phantoms, the orthogonal fibers with a larger SDSD are shown to be the more sensitive fiber geometry to the variants. The differences in the concentration and morphology of the stromal phantoms can be best manifested in the reflectance spectra when sufficient probing depths are achieved. On the other hand, the oblique fibers can effectively lessen or eliminate the stromal influence from the reflectance spectra and produce epithelial-specific spectra, despite the scattering conditions of the stromal phantom layer.

In the final part of this study, hemoglobin is the key element added to the tissue phantoms to provide biologically relevant absorption properties. The signs of strong hemoglobin absorption are evident in the reflectance spectra for all phantoms when the deeply probing 0-deg 500-μm fiber is used. Phantoms with different stromal layers are clearly discernable in direct viewing of the spectra. However, this fiber geometry fails to distinguish the epithelial layers of the phantoms that share a common stromal layer. As we shorten the fiber separation to 200 μm, several observations suggest an increase in the sensitivity to the superficial layer. We see from one such observation that the ratio of hemoglobin's Soret absorption at 415 nm to the rest of the spectra decreases, indicating that a reduction in hemoglobin absorption is most likely due to reduced path lengths and probing depths. Another significant finding is that the intensity variations of the measured reflectance, which were previously not discernable, can now be correlated to the scattering properties of the top layers. As such, phantoms with weaker epithelial scattering yield higher reflectance when measured at this particular fiber geometry (0 deg 200-μm), suggesting the onset of the influence of the upper layer in the presence of a dominating basal layer. However, despite the visible distinctions in the intensity levels of the reflectance spectra, the overlapping normalized spectra still reveal the insufficient resolution of the differences in the top layer using the orthogonal fiber geometry.

The transition from basal to superficial detection of phantom reflectance gradually evolves as the collection fiber angle is modulated to higher degrees. Complete layer separation is achieved when the fiber obliquity reaches 40 deg, for which only the oscillatory scattering characteristics of the top-layer polystyrene microspheres are seen. At the intermediate 20-deg collection angle, we find that the coarse structures of the overall spectra are still associated with the stromal phantoms. More specifically, the enhanced detection of early-returning photons using the 20-deg fibers causes phantoms with the common top layers to develop the same patterns of ripples that are specific to the microspheres embedded in their respective epithelial phantom layers. However, the grander peaks and valleys in their wave-like spectra are mismatched entirely. Interestingly, these peaks and valleys can be exactly matched when two phantoms with common stromal layers are compared, which indicates the residual presence of stromal reflectance in the spectra.

In conclusion, our study provides experimental evidence that spatially resolved reflectance spectroscopy can be achieved by the use of angularly variable fiber geometry. Based on the results of our phantom study, photons scattered from the epithelial phantom layer can be exclusively sampled using oblique fiber geometry. We also demonstrate that the absorption and scattering conditions in both superficial and basal layers of the phantoms can be selectively probed by using suitable combinations of fiber angles and separations. The angled fibers are sensitive to the changes of morphology (by spectral patterns) and concentration (by reflectance magnitude) of the scattering particles in either the epithelial or stromal layers of our phantoms when appropriate fiber geometry is selected. This is an encouraging result, since the morphological variations of the epithelial cells, which are often linked to the progression of epithelial dysplasia, may be accurately resolved using spatially resolved spectroscopy when this technique is further developed and matured in the future. An equally important observation is that hemoglobin absorption can be effectively assessed or excluded from the reflectance measurements. The findings of improved separation of tissue phantom layers and consequent increased sensitivity to phantom morphology and absorption may provide diagnostically vital insight for future implementation of spectroscopic methods for early cancer detection in actual epithelial tissue. With this study as a foundation, future efforts will focus on additional experimentation using *in-vitro* tissue samples coupled with the optimization of clinically applicable probe designs.

Acknowledgments

This work is supported by the Coulter Foundation. We thank C.K. Wang for his design of the adjustable multilayer phantoms. Additional thanks go to David Martin for his input and comments.

References

1. I. Bigio and J. R. Mourant, “Ultraviolet and visible spectroscopies for tissue diagnostics: fluorescence spectroscopy and elastic-scattering spectroscopy,” *Phys. Med. Biol.* **42**, 803–814 (1997).
2. K. Sokolov, R. Drezek, K. Gossage, and R. Richards-Kortum, “Reflectance spectroscopy with polarized light: is it sensitive to cellular and nuclear morphology,” *Opt. Express* **5** (13), 302–317 (1999).
3. R. Drezek, R. Richards-Kortum, M. Brewer, M. Feld, C. Pitris, A. Ferenczy, M. Faupel, and M. Follen, “Optical imaging of the cervix,” *2nd Intl. Conf. Cervical Cancer*, pp. 2015–2027 (2003).
4. A. Wax, J. W. Pythila, R. N. Graf, R. Nines, C. W. Boone, R. R. Dasari, M. S. Feld, V. E. Steele, and G. D. Stoner, “Prospective grading of neoplastic change in rat esophagus epithelium using angle-resolved low-coherence interferometry,” *J. Biomed. Opt.* **10** (5), 051604 (2005).
5. J. Mourant, T. Fuselier, J. Boyer, T. Johnson, and I. Bigio, “Prediction and measurements of scattering and absorption over broad wavelength range in tissue phantoms,” *Appl. Opt.* **36**, 949–957 (1997).
6. S. Avrillier, E. Tinet, D. Ettori, J. Tualle, and B. Gelebart, “Influence of emission-reception geometry in laser-induced fluorescence spectra from turbid media,” *Appl. Opt.* **37**, 2781–2787 (1998).
7. G. Kumar and J. Schmitt, “Optimal probe geometry for near-infrared spectroscopy of biological tissue,” *Appl. Opt.* **36**, 2286–2293 (1997).
8. T. J. Pfefer, L. Matchette, and R. Drezek, “Influence of illumination collection geometry on fluorescence spectroscopy in multi-layered tissue,” *Med. Biol. Eng. Comput.* **42**, 669–673 (2004).
9. T. J. Pfefer, K. Schomacker, M. Ediger, and N. Nishioka, “Multiple fiber probe design for fluorescence spectroscopy in tissue,” *Appl. Opt.* **41**, 4712–4720 (2002).
10. C. Zhu, Q. Liu, and N. Ramanujam, “Effect of fiber optic probe geometry on depth-resolved fluorescence measurements from epithelial tissues: a Monte Carlo simulation,” *J. Biomed. Opt.* **8** (2), 237–247 (2003).
11. T. J. Pfefer, L. Matchette, A. Ross, and M. Ediger, “Selective detection of fluorophore layers in turbid media: the role of fiber-optic probe design,” *Opt. Lett.* **28**, 120–122 (2003).
12. L. Quan and N. Ramanujam, “Relationship between depth of a target in a turbid medium and fluorescence measured by a variable-aperture method,” *Opt. Lett.* **27**, 102–106 (2002).
13. J. Mourant, J. Boyer, A. Hielscher, and I. Bigio, “Influence of the scattering phase function on light transport measurements in turbid media performed with small source-detector separations,” *Opt. Lett.* **21**, 546–548 (1996).
14. T. Papaioannou, N. Preyer, Q. Fang, A. Brightwell, M. Carnohan, G. Cottone, R. Ross, L. Jones, and L. Marcu, “Effects of fiber-optic probe design and probe-to-target distance on diffuse reflectance measurements of turbid media, an experimental and computational study at 337 nm,” *Appl. Opt.* **43**, 2846–2860 (2004).
15. D. Arifler, R. Schwarz, S. Chang, and R. Richards-Kortum, “Reflectance spectroscopy for diagnosis of epithelial precancer: model-based analysis of fiber-optic probe designs to resolve spectral information from epithelium and stroma,” *Appl. Opt.* **44**(20), 4291–305 (2005).
16. L. Nieman, A. Myakov, J. Aaron, and K. Sokolov, “Optical sectioning using a fiber probe with an angled illumination-collection geometry: evaluation in engineered tissue phantoms,” *Appl. Opt.* **43**(6), 1308–1319 (2004).
17. A. Wang, J. Bender, J. Pfefer, U. Utzinger, and R. A. Drezek, “Depth-sensitive reflectance measurements using obliquely oriented fiber probes,” *J. Biomed. Opt.* **10**(4), 044017 (2005).
18. M. Skala, G. Palmer, C. Zhu, Q. Liu, K. Vrotsos, C. Marshek-Stone, A. Gendron-Fitzpatrick, and N. Ramanujam, “Investigation of fiber-optic probe designs for optical spectroscopic diagnosis of epithelial pre-cancers,” *Lasers Surg. Med.* **34**, 25–38 (2004).
19. C. K. Brookner, M. Follen, I. Boiko, J. Galvan, S. Thomsen, A. Malpica, S. Suzuki, R. Lota, and R. Richards-Kortum, “Autofluorescence patterns in short-term cultures of normal cervical tissue,” *Photochem. Photobiol.* **71**, 730–736 (2000).
20. C. Sato, M. Shimada, Y. Yamada, and Y. Hoshi, “Extraction of depth-dependent signals from time-resolved reflectance in layered turbid media,” *J. Biomed. Opt.* **10**(6), 064008 (2005).
21. T. Collier, P. Shen, B. de Pradier, K. B. Sung, and R. Richards-Kortum, “Near real time confocal microscopy of amelanotic tissue: dynamics of aceto-whitening enable nuclear segmentation,” *Opt. Express* **6**(2), 40–48 (2000).
22. S. Chang, D. Arifler, R. Drezek, M. Follen, and R. Richards-Kortum, “Analytical model to describe fluorescence spectra of normal and preneoplastic epithelial tissue: comparison with Monte Carlo simulations and clinical measurements,” *J. Biomed. Opt.* **9**(3), 511–522 (2004).
23. G. Palmer and N. Ramanujam, “A Monte Carlo based inverse model for calculating tissue optical properties, part I: Theory and validation on synthetic phantoms,” *Appl. Opt.* **45**(5), 1062–1071 (2006).
24. K. Gossage, C. Smith, E. Kanter, L. Hariri, A. Stone1, J. Rodriguez, S. Williams, and J. Barton, “Texture analysis of speckle in optical coherence tomography images of tissue phantoms,” *Phys. Med. Biol.* **51**, 1563–1575 (2006).
25. V. Backman, V. Gopal, M. Kalashnikov, K. Badizadegan, R. Gurjar, A. Wax, I. Georgakoudi, M. Mueller, C. Boone, R. Dasari, and M. Feld, “Measuring cellular structure at submicrometer scale with light scattering spectroscopy,” *IEEE J. Quantum Electron.* **7**(6), 887–893 (2001).
26. V. Backman, M. Wallace, L. Perelman, J. Arendt, R. Gurjar, M. Muller, Q. Zhang, G. Zonios, E. Kline, T. McGillican, S. Shapshay, T. Valdez, K. Badizadegan, J. Crawford, M. Fitzmaurice, S. Kabani, H. Levin, M. Seiler, R. Dasari, I. Itzkan, J. Van Dam, and M. Feld,

"Detection of preinvasive cancer cells," *Nature (London)* **406**, 35–36 (2000).

27. V. Backman, R. Gurjar, K. Badizadegan, I. Itzkan, R. Dasari, L. Perelman, and M. Feld, "Polarized light scattering spectroscopy for quantitative measurements of epithelial cellular structures in situ," *IEEE J. Quantum Electron.* **5**, 1019–1026 (1999).
28. R. Gurjar, V. Backman, L. Perelman, I. Georgakoudi, K. Badizadegan, I. Itzkan, R. Dasari, and M. Feld, "Imaging human epithelial properties with polarized light-scattering spectroscopy," *Nat. Med.* **7**(11), 1245–1248 (2001).
29. K. J. Heppner, L. M. Matrisian, R. A. Jensen, and W. H. Rodgers, "Expression of most matrix metalloproteinase family members in breast cancer represents a tumor-induced host response," *Am. J. Pathol.* **149**, 273–282 (1996).
30. W. C. Parks, *Matrix Metalloproteinases* Academic, San Diego, CA (1998).
31. I. Pavlova, K. Sokolov, R. Drezek, A. Malpica, M. Follen, and R. Richards-Kortum, "Microanatomical and biochemical origins of normal and precancerous cervical autofluorescence using laser-scanning fluorescence confocal microscopy," *Photochem. Photobiol.* **77**, 550–555 (2003).
32. I. Georgakoudi, E. Sheets, M. Müller, V. Backman, C. Crum, K. Badizadegan, R. Dasari, and M. Feld, "Trimodal spectroscopy for the detection and characterization of cervical percancers *in vivo*," *Am. J. Obstet. Gynecol.* **186**, 374–382 (2002).
33. M. Müller, T. Valdez, I. Georgakoudi, V. Backman, C. Fuentes, S. Kabani, N. Laver, Z. Wang, C. Boone, R. Dasari, S. Shapshay, and M. Feld, "Spectroscopic detection and evaluation of morphologic and biochemical changes in early human oral carcinoma," *Cancer* **97**, 1681–1692 (2003).
34. A. Amelink, M. Bard, S. Burgers, and T. Sterenborg, "Single-scattering spectroscopy for the endoscopic analysis of particle size in superficial layers of turbid media," *Appl. Opt.* **42**(19), 4095–4101 (2003).
35. A. Amelink and T. Sterenborg, "Measurement of the local optical properties of turbid media by differential path-length spectroscopy," *Appl. Opt.* **43**(15), 3048–3054 (2004).
36. D. Arifler, C. MacAulay, M. Follen, and R. Richards-Kortum, "Spatially resolved reflectance spectroscopy for diagnosis of cervical precancer: Monte Carlo modeling and comparison to clinical measurements," *J. Biomed. Opt.* **11**(6), 064027 (2006).
37. Q. Liu and N. Ramanujam, "Experimental proof of the feasibility of using an angled fiber-optic probe for depth-sensitive fluorescence spectroscopy of turbid media," *Opt. Lett.* **29**(17), 2034–2036 (2004).
38. R. Schwarz, D. Arifler, S. Chang, I. Pavlova, I. Hussain, V. Mack, B. Knight, R. Richards-Kortum, and A. Gillenwater, "Ball lens coupled fiber-optic probe for depth resolved spectroscopy of epithelial tissue," *Opt. Lett.* **30**(10), 1159–1161 (2005).
39. A. Wang, V. Nammalvar, and R. Drezek, "Targeting spectral signatures of progressively dysplastic stratified epithelia using angularly variable fiber geometry in reflectance Monte Carlo simulations," *J. Biomed. Opt.* **12**, 044013 (2007).